ADVANCED MATERIALS
www.advmat.de

A Self-Powered UV Photodetector With Ultrahigh Responsivity Based on 2D Perovskite Ferroelectric Films With Mixed Spacer Cations

Linjuan Guo, Yaqian Qi, Zihao Wu, Xiaoran Yang, Guoying Yan, Ridong Cong, Lei Zhao, Wei Zhang, Shufang Wang, Caofeng Pan,* and Zheng Yang**

Self-powered photodetectors (PDs) have the advantages of no external power requirement, wireless operation, and long life. Spontaneous ferroelectric polarizations can significantly increase built-in electric field intensity, showing great potential in self-powered photodetection. Moreover, ferroelectrics possess pyroelectric and piezoelectric properties, beneficial for enhancing self-powered PDs. 2D metal halide perovskites (MHPs), which have ferroelectric properties, are suitable for fabricating high-performance self-powered PDs. However, the research on 2D metal halide perovskites ferroelectrics focuses on growing bulk crystals. Herein, 2D ferroelectric perovskite films with mixed spacer cations for self-powered PDs are demonstrated by mixing Ruddlesden–Popper (RP)-type and Dion–Jacobson (DJ)-type perovskite. The $(BDA_{0.7}(BA_2)_{0.3})(EA)_2Pb_3Br_{10}$ film possesses, overall, the best film qualities with the best crystalline quality, lowest trap density, good phase purity, and obvious ferroelectricity. Based on the ferro–pyro–phototronic effect, the PD at 360 nm exhibits excellent photoelectric properties, with an ultrahigh peak responsivity greater than 93 A W^{-1} and a detectivity of 2.5×10^{15} Jones, together with excellent reproducibility and stability. The maximum responsivities can be modulated by piezo–phototronic effect with an effective enhancement ratio of 480%. This work will open up a new route of designing MHP ferroelectric films for high-performance PDs and offers the opportunity to utilize it for various optoelectronics applications.

1. Introduction

Photodetectors (PDs) are widely used in various fields of the national economy and military, such as environmental monitoring, image sensing, and automatic industrial control.[1,2] Self-powered PDs have the advantages of no external power requirement, wireless operation, and long life, and so, can be used in low-energy optoelectronic fields,[3,4] such as wireless environmental sensing, intelligent wearable chemical and biological sensing, and human–machine interface. Among the multiple methods that can enhance the performance of the self-powered PDs, spontaneous ferroelectric polarizations in photo–ferroelectrics can significantly increase the built-in electric field intensity; thus, effectively separating the photogenerated carriers, showing great potential in self-powered photodetection.[5–7] Ferroelectrics also possess pyroelectric and piezoelectric properties. The overall performance of self-powered PDs can be significantly improved by utilizing the pyro–phototronic effect, a three-way coupling effect among pyroelectricity, photoexcitation, and semiconductors[8–12] or piezo–phototronic effect[13–15] because polarized charges at the interfaces can modulate the photoelectric process. However, traditional inorganic ferroelectrics such as $BaTiO_3$ show poor photoelectric properties, which are unsuitable for high-performance PDs. Developing semiconducting materials with synergy and coupling functions of excellent ferroelectric and photoelectric properties is still challenging.

Recently, metal halide perovskites (MHPs) such as $MAPbI_3$ have become ideal materials for constructing optoelectronic devices such as solar cells, light-emitting diodes, and PDs due to their high absorption coefficient, low defect density, high mobility, and high tolerance to defects.[16–19] Further, some MHPs possess ferroelectric properties while maintaining excellent photoelectric properties,[20,21] which are very suitable for fabricating self-powered PDs. However, 3D perovskites usually suffer from poor chemical and structural stability.[22] On the contrary, 2D perovskites with a structural formula of $L_2A_{n-1}M_nX_{3n+1}$ (Ruddlesden–Popper, RP-type) or

L. Guo, Y. Qi, Z. Wu, X. Yang, G. Yan, R. Cong, L. Zhao, W. Zhang, S. Wang, Z. Yang
Hebei Key Laboratory of Optic-Electronic Information and Materials
National & Local Joint Engineering Laboratory of New Energy Photoelectric Devices
College of Physics Science and Technology
Hebei University
Baoding 071002, P. R. China
E-mail: sfwang@hbu.edu.cn; yangzheng06@hbu.edu.cn

L. Guo, C. Pan, Z. Yang
CAS Center for Excellence in Nanoscience
Beijing Institute of Nanoenergy and Nanosystems
Chinese Academy of Sciences
Beijing 100140, P. R. China
E-mail: cfpan@binn.cas.cn

The ORCID identification number(s) for the author(s) of this article can be found under https://doi.org/10.1002/adma.202301705

DOI: 10.1002/adma.202301705

$L"A_{n-1}M_nX_{3n+1}$ (Dion–Jacobson, DJ-type), where L is mono ammonium cation; $L"$ is diammonium cation; A is small cations such as MA^+; M is Pb^{2+}, Sn^{2+}or Ge^{2+}; X is halide; and n is the number of inorganic layers formed by the $[MX_6]$ octahedron between two long chains,[23,24] have higher structural stability, chemical stability, and good flexibility, suitable for fabricating high-performance PDs.[25–27] More importantly, the synergistic effect of the ordered arrangement of organic components in 2D MHPs and the relative displacement of the octahedron $[MX_6]$ make them easier to generate spontaneous polarizations.[28] Currently, a variety of 2D MHPs has been confirmed to show ferroelectric properties.[29–33]

Currently, the research on 2D MHPs ferroelectrics focuses on growing bulk crystals, whose time-consuming, uncontrollable, and small-scale growth procedures result in poor reproducibility of the devices. From the perspective of industrialization, the large-scale and repeatable growth of 2D ferroelectric MHP films has become a key research focus. However, the disordered arrangement of organic layers[34,35] and the random well-width distribution (n value)[36] in 2D perovskite films will significantly reduce the optoelectronic properties of the entire devices, as well as the spontaneous polarizations. Therefore, controlling the phase purity and orientation of the 2D MHPs films is critical to obtaining excellent ferroelectric and photoelectric properties. Our previously reported work demonstrated the RP phase perovskite ferroelectric films for self-powered PDs.[37] However, the nonuniform distribution of the RP films' quantum wells makes it hard to achieve higher photosensing performance and thermal stability. Owing to the shorter interlayer distance, the DJ phase perovskites exhibit better thermal stability and more uniform quantum wells than the RP phase perovskites. Therefore, it is essential to balance the structural rigidity, phase purity, and defect-tolerance capability of the 2D perovskite[38,39] by mixing the two types of 2D MHPs, which is beneficial for guaranteeing the ferroelectric and photoelectric properties.

Herein, we demonstrate 2D ferroelectric perovskite films with mixed spacer cations for self-powered PDs. The rigid divalent DJ-type spacer cation of 1,4-butanediamonium (BDA^{2+}) is incorporated into the n-butylammonium (BA^+)-based RP-type perovskite matrix, resulting in the $(BDA_x(BA_2)_{1-x})(EA)_2Pb_3Br_{10}$ ($0\leq x \leq 1$) 2D ferroelectric perovskite films. The introduction of the BDA^{2+} spacer cations greatly influences the film properties, including phase distribution, defect density, photoelectric performance, and stability, while maintaining ferroelectric properties. The $(BDA_{0.7}(BA_2)_{0.3})(EA)_2Pb_3Br_{10}$ film possesses, overall, the best film qualities. Further, self-powered UV PDs based on 2D perovskite/PC61BM heterojunction are fabricated. Significantly, based on the ferro–pyro–phototronic effect, $(BDA_{0.7}(BA_2)_{0.3})(EA)_2Pb_3Br_{10}$ film-based PD at 360 nm exhibits excellent photoelectric properties, with a dark current of less than 3×10^{-12} A, an ultrahigh peak responsivity of more than 93 A W^{-1}, a detectivity of 2.5×10^{15} Jones, and rise/fall times in the microsecond level, together with the excellent reproducibility and stability. After applying pressures to the PDs, the maximum responsivities can be modulated by the piezo–phototronic effect with an effective enhancement ratio of 480%. Our work will open up a new route of designing MHP ferroelectrics for high-performance PDs and offers the opportunity to utilize it for various applications, including photoelectric synapse, neuromorphic vision sensors, and emergency alert systems.

2. Results and Discussion

The multiple-quantum-well structures in RP MHP films limit the performances of the RP MHP-based optoelectronic devices. It is expected to prepare high-quality films with narrower phase distribution and improved carrier transport by mixing the proper amount of the DJ phase with the RP phase. To guarantee the ferroelectricity of the as-prepared films with different compositions, a typical RP-type ferroelectric MHP with the nominal composition of $BA_2EA_2Pb_3Br_{10}$[40] and DJ-type ferroelectric MHP with the nominal composition of $(BDA)(EA)_2Pb_3Br_{10}$[31] were selected to prepare the mixed 2D perovskite ferroelectric films because they possess the same small cation (EA^+, ethylamine), halide ion (Br^-), and n number ($< n > = 3$). The chemical formula of the 2D films with mixed spacer cations is described as $(BDA_x(BA_2)_{1-x})(EA)_2Pb_3Br_{10}$, where $x = 0$ or 1 corresponds to pure RP or DJ phase perovskite film, and $x = 0.6$, 0.7, 0.8, and 0.9 corresponds to the mixed perovskite films. The 2D perovskite films made from pure DJ or RP phase film, and the mixed films with different ratios are defined as BA_2, $BDA_{0.6}$, $BDA_{0.7}$, $BDA_{0.8}$, $BDA_{0.9}$, and BDA, respectively.

As shown in **Figure 1**a, a one-step spin-coating method under a constant heating temperature (70 °C) was used to prepare the 2D MHP films in the ambient environment (24 °C, 35 ± 10 RH%), which overcame the dependence of the glove box. An additive of methanamine acetate (MAAc) ionic liquid was introduced into the precursor solution after the complete dissolution of the salts because acetate (Ac^-) can form a strong ionic coordination with the perovskite framework;[36,41] thus, regulating the orientation and phase purity of the perovskite crystalline grains. The optimized ratio of MAAc to EA^+ was determined to be 1:1. First, the microscopic morphologies of the six perovskite films were investigated via scanning electron microscopy (SEM). From the top-view SEM images in Figure S1, Supporting Information, all six films show smooth surfaces and full coverage on the substrates, with a large average grain size of ≈3 µm, among which $BDA_{0.7}$ film shows the fewest pinholes. Specifically, the introduction of the BDA^{2+} makes the films' grain boundaries difficult to distinguish, reducing the invading pathways of humidity and oxygen. Figure S2, Supporting Information shows the cross-sectional SEM images of the six perovskite films. Some small voids were found in the interface between BA_2 and $BDA_{0.6}$ perovskite films and ITO electrodes. While the proportion of BDA^{2+} was not less than 0.7, voids were no longer seen in the perovskite films, demonstrating the good contact between the perovskite film and ITO electrodes. Besides, all the films demonstrated identical monolithic grains from top to bottom, with the thickness ranging from 250 to 280 nm. The 2D perovskite films with excellent crystallinity and close contact with the substrates induced by BDA^{2+} doping were highly suitable for optoelectronic devices. As the degree of vertical growth orientation significantly affects the carrier transport characteristics of the 2D MHP, the crystallographic structures of the perovskite films were first studied by X-ray diffraction (XRD) patterns. Figure 1b shows the XRD patterns of the six films. The BA_2 film displays eight diffraction peaks, with two strong diffraction peaks at 14.2° and 28.45°,

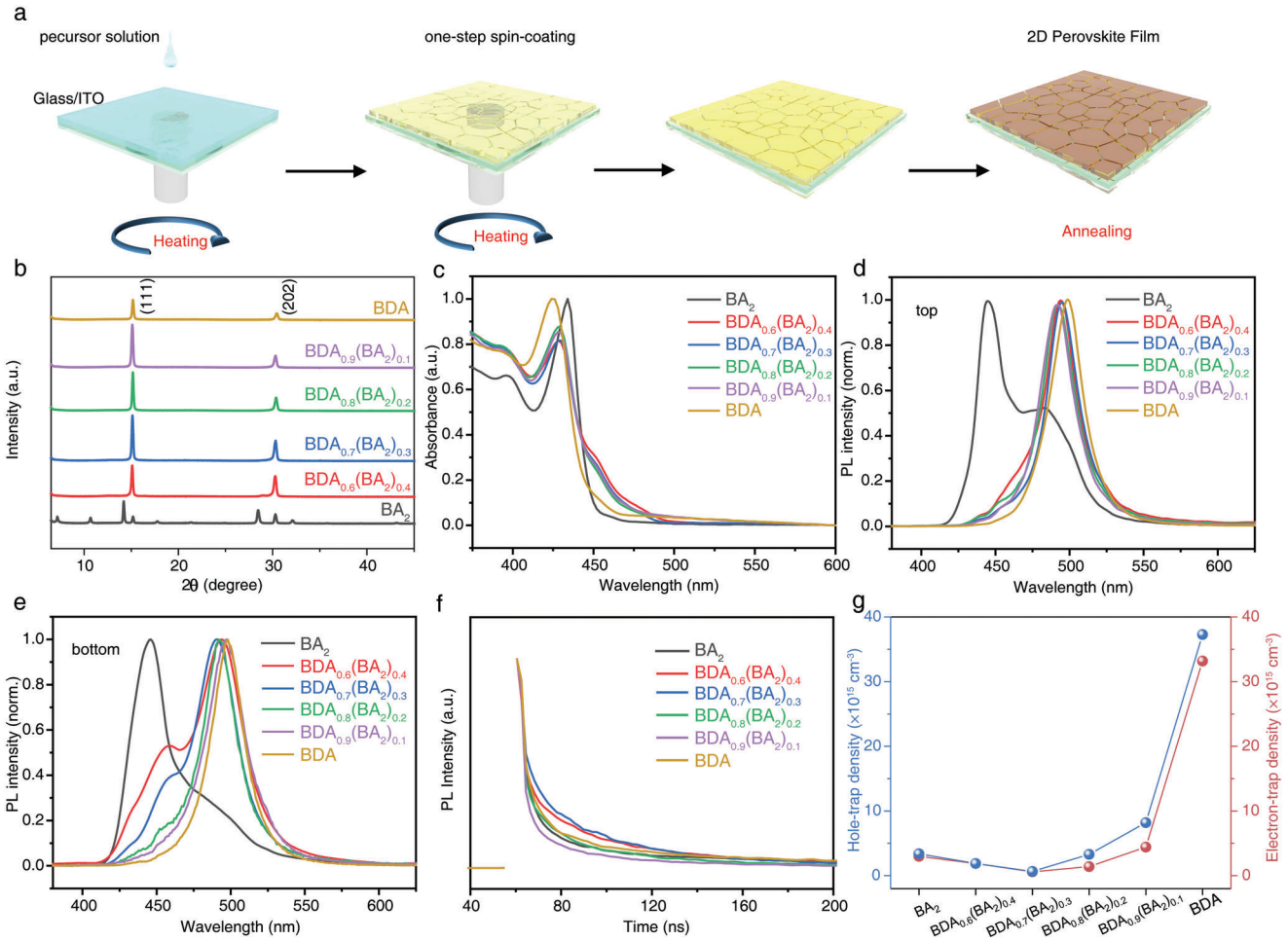

Figure 1. Characterizations of the BA_2, $BDA_{0.6}$, $BDA_{0.7}$, $BDA_{0.8}$, $BDA_{0.9}$, and BDA perovskite films. a) Schematic diagram of the one-step spin-coating method to prepare the 2D perovskite films. b) XRD patterns, c) absorption spectra, steady-state PL spectra excited from d) top side and e) bottom side, f) time-resolved PL decay curves, and g) trap densities for the hole and electron of the BA_2, $BDA_{0.6}$, $BDA_{0.7}$, $BDA_{0.8}$, $BDA_{0.9}$, and BDA perovskite films.

which are attributed to (040) and (080) crystallographic planes of 2D perovskite. The diffraction peaks at 15.2° and 30.3°, responding to (111) and (202) crystal planes, also exist. The multiple peaks belonging to different crystal planes indicate the random crystal orientation of the pure RP BA_2 film. While for mixed films and pure DJ BDA film, all the five films exhibit only two obvious diffraction peaks at 15.2° and 30.3°, responding to (111) and (202) crystal planes, respectively. Generally, the (111) and (202) crystal planes denote the inorganic [*MX*6] octahedral layer perpendicular and inclined to the substrate, respectively.[42–44] The higher (202)/(111) diffraction intensity ratio means the more vertical orientation of 2D perovskite to the substrate. Among the BDA-based films, $BDA_{0.7}$ film maintains the highest diffraction intensity, minimum full width at half maximum, and highest (202)/(111) diffraction intensity ratio of 0.477 (0.375 for $BDA_{0.8}$ film, 0.278 for $BDA_{0.9}$ film, and 0.265 for BDA film), demonstrating the enhanced crystallinity and improved growth orientation toward the out-of-plane direction. Further increasing the content of BDA^{2+} would lead to the decreased intensity of diffraction peaks. Properly mixing the proportion of flexible BA^{+} cations and rigid BDA^{2+} cations could ease the lattice distortions and enhance the film quality. To further determine the crystal orientation of the films relative to the substrate, grazing incidence wide-angle X-ray scattering (GIWAXS) measurements were performed on the three typical films (BA_2, $BDA_{0.7}$, and BDA). Figure S3a, Supporting Information for the BA_2 film demonstrates arc-like peaks corresponding to (060), (080), and (0100) planes, indicating partially ordered crystallographic orientation. Besides, diffraction ring-like scattering signals of the (111) plane were observed, indicating considerable randomness of the crystalline orientation, which agrees well with the X-ray diffraction results. The GIWAXS images for $BDA_{0.7}$ and BDA films were similar, with sharp ellipse-like signals such as (111), (002), and (202) diffractions, suggesting much-enhanced crystallinity and preferential vertical orientation, offering an efficient carrier-transport channel between the two electrodes, favorable for high-performance PDs. The XRD and GIWAXS results proved that mixing DJ-type perovskite with RP-type perovskite can effectively regulate the crystal grain orientations in the films. Besides, the phase purity of the 2D perovskite films is critical for the ferroelectricity and photoelectric properties. Therefore, the six films' UV–visible absorption and photoluminescence (PL) spectra were measured.

As shown in Figure 1c, the BA_2 film exhibits exciton peaks at ≈400 nm ($n = 2$) and 433 nm ($n = 3$), while the BDA film exhibits only one exciton peak at ≈425 nm ($n = 3$), showing its high phase purity. A main exciton peak at 428.5 nm ($n = 3$) is observed for the four mixed films, along with a weaker peak at 450 nm ($n = 4$), demonstrating the different phase distribution among pure RP film, mixed films, and pure DJ film. No exciton absorption peaks for $n = \infty$ are found for all of the six films. More obvious differences among different films can be found from the PL spectra excited from the top and bottom sides of films (Figure 1d,e). For BA_2 film, obvious PL peaks at 445 nm ($n = 2$) and 483 nm ($n = 3$) are observed when excited from the top side. In contrast, the PL peaks for BDA-based films differ quite from that of the BA_2 one. Only peaks at ≈495 nm ($n = 4$) can be found when excited from the top. For the bottom condition, the PL spectrum of the BA_2 film is similar to the top condition. Two peaks at ≈457 nm ($n = 3$) and 495 nm ($n = 4$) are observed for the mixed films when excited from the bottom side. With the increase of the BDA^{2+} content, the intensity of the peaks for $n = 3$ gradually decreases, demonstrating the enhanced phase purity or more uniform distribution of the quantum well's widths. Time-resolved photoluminescence (TRPL) measurements were performed to analyze the fluorescence carrier dynamics of perovskite films (Figure 1e). By a double exponential decay fitting of the TRPL curves, the PL lifetimes of the different films could be obtained, with the smaller one corresponding to surface recombination and the larger one corresponding to bulk recombination. All the lifetimes are listed in Table S1, Supporting Information. The lifetimes of 2 and 40 ns were measured for $BDA_{0.7}$ film, significantly longer than those of other films, demonstrating the lowest defect density and highest film quality of $BDA_{0.7}$ film. Then, the trap densities of the six 2D perovskite films were measured via a space charge limited current (SCLC) method by fabricating both hole-only devices and electron-only devices; and thus, measuring the dark current–voltage (I–V) curve (Figure S4, Supporting Information). The trap densities could be calculated according to the following equation:

$$n_{\text{trap}} = \frac{2\epsilon_0 \epsilon_r V_{\text{TFL}}}{eL^2} \tag{1}$$

where ϵ_0 is the vacuum permittivity, ϵ_r is the relative dielectric constant, V_{TFL} is the trap-filled limit voltage, e is the electron charge, and L is the film thickness. Here, ϵ_r was calculated according to the equation:

$$\epsilon_r = \frac{C_g L}{\epsilon_0 A} \tag{2}$$

where C_g is geometric capacitance, L is the film thickness, ϵ_0 is the vacuum permittivity, and A is the effective area of devices. The C_g was determined from the capacitance–frequency measurements plotted in Figure S5, Supporting Information. Therefore, the six films' calculated trap densities for holes and electrons were plotted in Figure 1g. The trap densities of mixed film (6×10^{14} cm^{-3} for electrons and 6.6×10^{14} cm^{-3} for holes) were much lower than those for BDA and BA-based films (Table S2, Supporting Information), meaning lower non-radiative recombination rates.

From the characterizations above, one can see that the $BDA_{0.7}$ film showed the best crystallinity, the lowest trap density, favorable orientation, and phase purity. However, as MA^+ from MAAc exists in the precursor solution, perovskite films with mixed MA^+ and EA^+ cations may be obtained. Therefore, the actual components in the $BDA_{0.7}$ film were determined via the 1H nuclear magnetic resonance (1HNMR) spectroscopy. Figure S6, Supporting Information shows the signals of chemical shift peaks belonging to MA^+ and EA^+ in the film, with the area ratio of 0.16: 1, namely, the component ratio of MA^+ and EA^+. Therefore, the composition of $BDA_{0.7}$ film may be $(BDA_{0.7}BA_{0.6})(EA)_{1.7}(MA)_{0.3}Pb_3Br_{10}$. To determine the role of MAAc, we also prepared the $BDA_{0.7}$ film without MAAc, and with different levels of MAAc. From the XRD patterns in Figure S7a, Supporting Information, one can see that the introduction of MAAc can enhance crystallinity. MAAc can also greatly influence the phase distribution of 2D perovskite. As shown in Figure S7b, Supporting Information, for $BDA_{0.7}$ film without MAAc, four PL peaks at 440 nm ($n = 2$), 473 nm ($n = 3$), 497 nm ($n = 4$), and 522 nm ($n = 5$) are observed when excited from the top side, demonstrating much lower phase purity than the MAAc-based one. Moreover, the content of MAAc in precursor solution plays an important role in controlling phase distribution. Excessive or insufficient MAAc will change phase distribution, generating non-ferroelectric phases (Figure S8, Supporting Information). Finally, the $BDA_{0.7}$ film with MAAc: EA^+ = 1:1 was selected for further in-depth study. Then, the overall properties of the $BDA_{0.7}$ film were systematically studied. First, the energy level distributions of the $BDA_{0.7}$ film from top to bottom were determined from the ultraviolet photoelectron spectroscopy (UPS) measurements. From the UPS spectra in **Figure 2**a, the valence band edge position of the film top surface at −6.56 eV and fermi level at −4.84 eV were estimated, respectively, relative to the vacuum level. As the 2D phase belonging to $n = 4$ existed at the film's top surface, the conduction band edge position at −3.98 eV could be determined. Further, the Fermi level and valence band of the $BDA_{0.7}$ film at different depths could be determined by etching the films with Ar plasma and conducting the UPS measurements. When the etching depth was less than 60 nm, the Fermi level and valence band gradually decreased with the increased depth, forming a gradient energy level. When further increasing the etching depth, the Fermi level and valence band almost remained unchanged, consistent with the results of optical characterizations, indicating phase homogeneity within the film. The corresponding X-ray photoelectron spectra (XPS) for Pb and Br are shown in Figure S9, Supporting Information, with no obvious peak for Pb^0, proving the bromine vacancy-free feature of the perovskite films. To further testify to the phase purity of the $BDA_{0.7}$ film, the ultrafast transient absorption (TA) spectroscopy was employed to determine the phase distributions from both the top side (perovskite film side) and the bottom side (substrate side) with an excitation wavelength at 360 nm. A main bleaching peak was located at 426 nm ($n = 3$) for the bottom side (Figure 2c; Figure S10a, Supporting Information), while two peaks located at 426 nm ($n = 3$) and 451 nm ($n = 4$) were observed for the top (Figure 2d; Figure S10b, Supporting Information). The TA results indicate the uniform quantum well distribution from the bottom to the top of the perovskite films, consistent with the PL and UPS results. The phase purity (ferroelectric phase, $n = 3$) of the

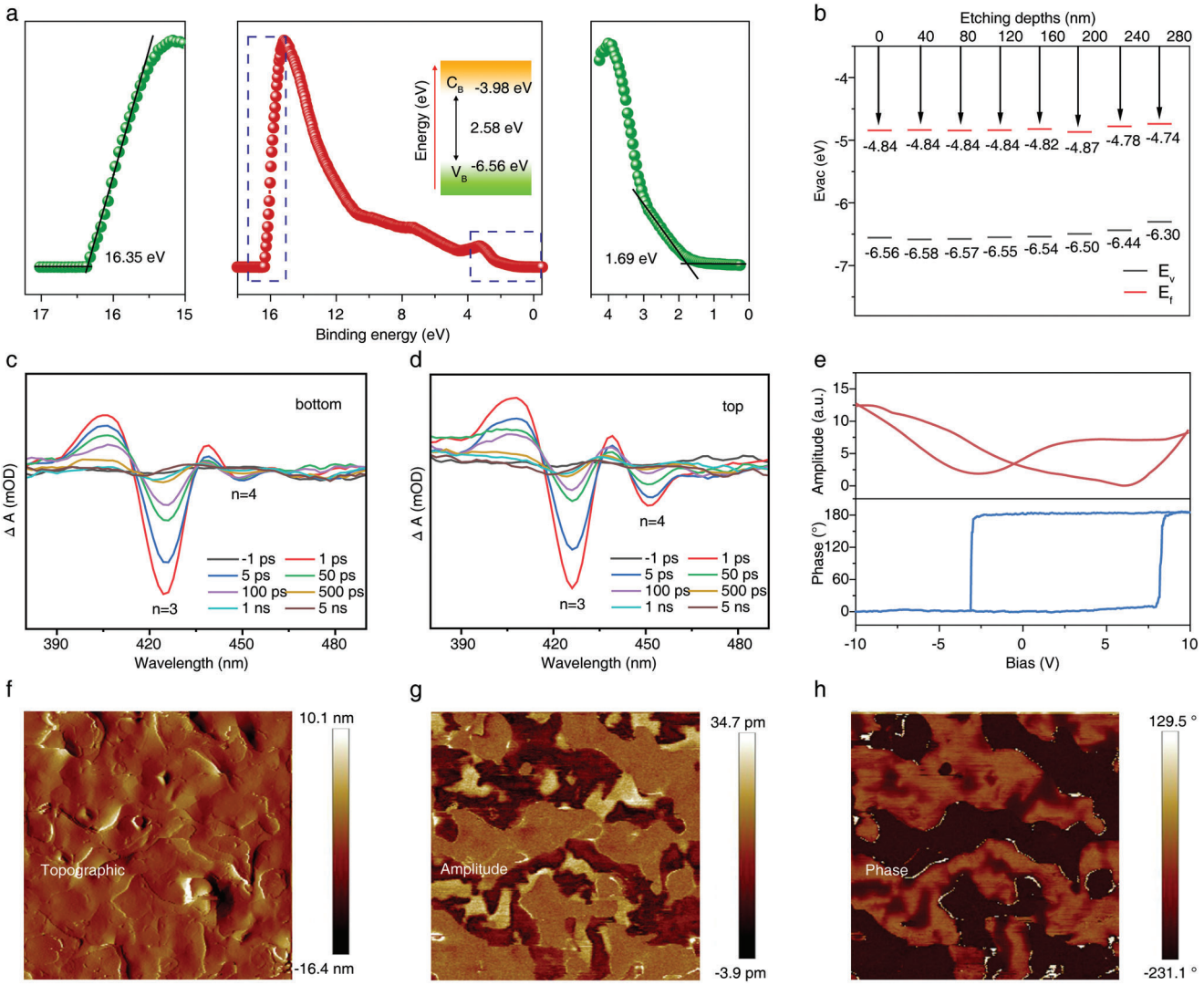

Figure 2. Optical and electrical properties of the $BDA_{0.7}$ film. a) UPS spectra of the top side of the $BDA_{0.7}$ film. b) Energy level diagram of $BDA_{0.7}$ film with different etching depths (from 0 to 280 nm). The TA spectra of BDA0.7 film are excited from the c) bottom side and d) top side. e) Out-of-plane PFM hysteresis loops measured in the film surface, showing a hysteresis loop and a butterfly curve. f) Topographic image, g) amplitude image, and h) PFM phase image of the $BDA_{0.7}$ film.

films would ensure the ferroelectric property of the 2D films. To confirm the ferroelectricity of the three films (BA_2, $BDA_{0.7}$, and BDA), polarization-electric field (P–E) hysteresis loops were carried out (Figure S11, Supporting Information). All three curves showed typical ferroelectric behaviors with both residual polarizations (P_r) and strong coercive fields (E_C) along the vertical direction from ITO to the top electrode, which provides the basis for the ferro–pyro–phototronic effect. Further, piezoresponse force microscopy (PFM) measurements were conducted to investigate the ferroelectric properties of $BA_{0.7}$ film. As shown in Figure 2e, a typical hysteresis loop and a butterfly loop obtained by out-of-plane PFM demonstrate the polarization switching of ferroelectric domains. The topographic image of the $BDA_{0.7}$ film shows smooth and pinhole-free surface characteristics (Figure 2f). The corresponding amplitude and phase images obtained with vertical PFM mode are shown in Figure 2g,h. The out-plane ferroelectric domains with different polarization orientations can be distinguished by the clear color contrast (reddish yellow and dark brown colors) with clear domain walls showing a phase difference of ≈180°. In addition, the same domain textures can be observed in amplitude images. To testify the Curie temperature of the $BDA_{0.7}$ film, the temperature-dependent dielectric constant and P–E hysteresis loops measurements were also conducted. As shown in Figure S12, Supporting Information, the dielectric constant ϵ shows a significant peak at 371 K, which demonstrates the ferroelectric–paraelectric phase transition. In addition, Figure S13a, Supporting Information shows the P–E loops of the $BDA_{0.7}$ film obtained at 298, 332, and 373 K. For the 298 and 332 K, the Ps were estimated to be 2.05 and 1.37 μC cm^{-2}, respectively. While for 373 K, the loops were closed, further confirming the ferroelectric to paraelectric phase transition at Curie temperature. The temperature dependent P_s obtained from P–E loops was plotted

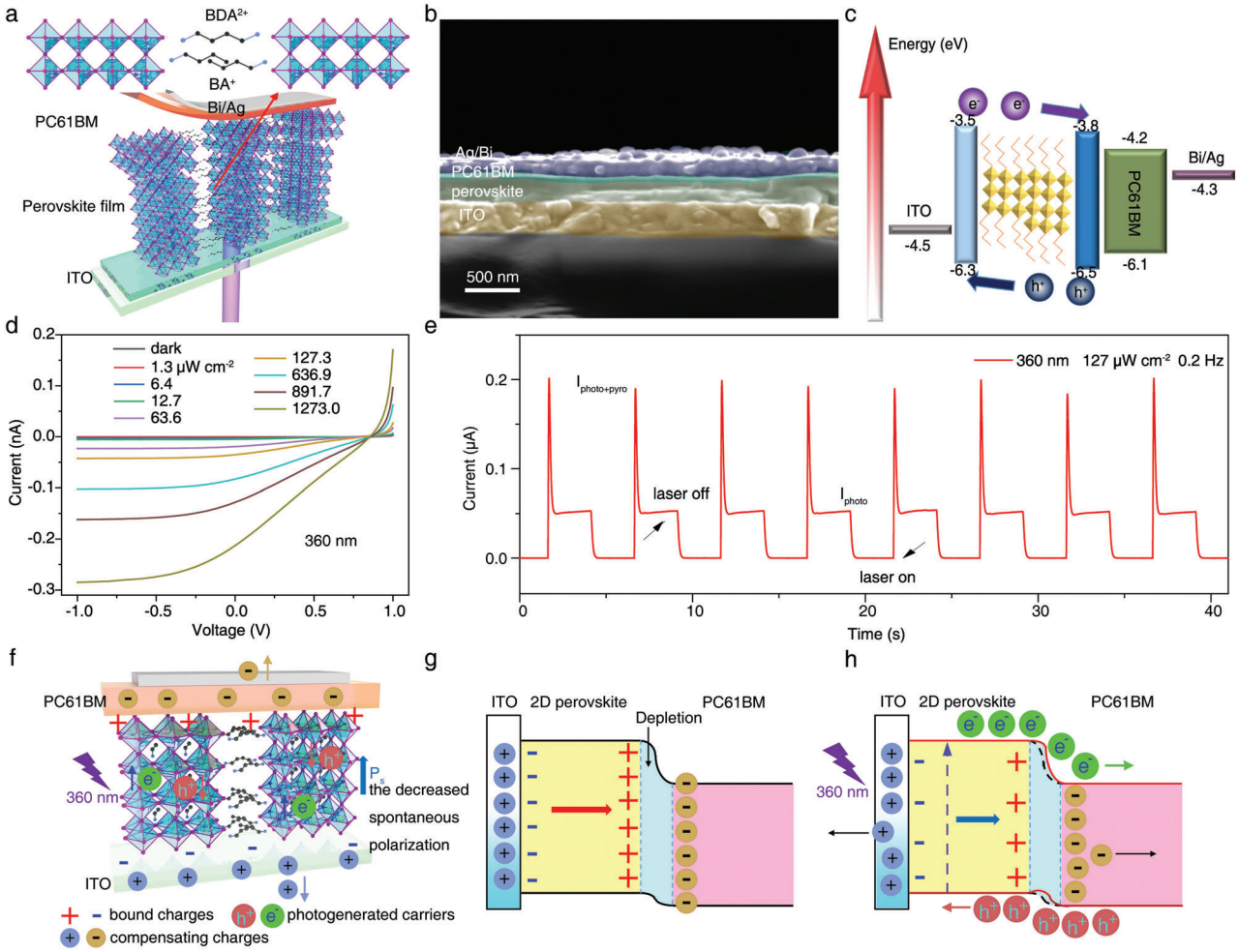

Figure 3. The working mechanism of the self-powered PDs. a) The schematic diagram showing the device structure. Inset: chemical structure of BA^+ and BDA^{2+}. b) Cross-sectional SEM images of the PD based on the $BDA_{0.7}$ film. c) Energy band diagram of the PD. d) *I–V* characteristics under 360 nm laser with different power densities ranging from 0 to 1273 μW cm^{-2}. e) *I–t* characteristics of the PD under 360 nm laser, showing typical pyroelectric and photoelectric responses. f) The schematic diagram of the fundamental working mechanism of ferro–pyro–phototronic effect-based self-powered PDs. Energy band diagrams of the self-powered PD at g) equilibrium state and h) under 360 nm illumination conditions.

as a function of temperature in Figure S13b, Supporting Information. With the increase of the temperature, the P_s gradually decreased, reaching 0 at 372 K. As the pyroelectric coefficient is the gradient of the polarization versus temperature, the theoretical pyroelectric coefficient was calculated from Figure S13a, Supporting Information. The corresponding pyroelectric coefficient as a function of temperature is also plotted in Figure S13b, Supporting Information. All the above results prove the presence of ferroelectricity in the mixed film. The spontaneous polarization of the mixed film was derived from the orderly arrangement of the positive cations (EA^+, BA^+, and BDA^{2+}), leading to symmetry breaking. Such ordering of the dynamic three positive cations enabled the rearrangement of the molecular dipoles and facilitated the generation of electric polarization, resulting in significant ferroelectricity. Therefore, the mixed film with low trap density, high phase purity, and good ferroelectricity was suitable for fabricating high-performance self-powered PDs.

Then, the BA_2, $BDA_{0.7}$, and BDA films were fabricated into the self-powered PDs with a structure of ITO/2D perovskite/PC61BM/Bi/Ag (PDs with mixed cations are schematically illustrated in **Figure 3**a). The cross-view SEM image of a $BDA_{0.7}$ film-based PD is presented in Figure 3b, with corresponding energy levels of each component in self-powered PD shown in Figure 3c. Before photoresponse measurements, a polarization voltage of 1 V was applied to the PDs for 1 min, with the polarization direction pointing to PC61BM; namely, the positive pole was connected to ITO, while the negative pole was connected to the Ag electrode. Here, a bias of 1 V was used because the output pyroelectric currents tend to become saturated when further increasing the polarization voltage (Figure S14, Supporting Information). Figure 3d shows the *I–V* curves of $BDA_{0.7}$ film-based PDs measured in the dark and under 360 nm laser illumination with different power densities ranging from 1.3 to 1273 μW cm^{-2}, with apparent rectifying behavior, high open-circuit voltage, and short-circuit current, demonstrating the self-powered photodetection ability. A 360 nm laser was chosen as the primary light source because the PDs showed the highest photoresponse toward the 360 nm laser (Figure S15, Supporting

Information). Moreover, all the photoresponses demonstrate the typical pyroelectric photo-response behaviors for the seven wavelengths ranging from 320 to 1064 nm. Further, we evaluated the light-induced temperature change of the $BDA_{0.7}$ film using an infrared camera. Figures S16–S20, Supporting Information show the thermal images of the $BDA_{0.7}$ film coated on quartz slice illuminated with 320, 360, 405, 532, and 785 nm lasers, respectively, all showing temperature rise when increasing the laser illumination power. As shown in Figure S21, Supporting Information, under laser illumination with the same power (120 μW), a temperature change of 6 °C was obtained for 360 nm, much higher than other wavelengths. In addition, no significant differences were found when lasers were illuminated on to the top surface or bottom surface (quartz slice side). When photons of sufficient energies excited the perovskite, electron–hole pairs were generated with energies surpassing the bandgap. In semiconductors, the recombination of charge carriers can result in the release of phonons instead of photons, leading to increased heat loss and a subsequent rise in local lattice temperature.[45] Higher excess energies correspond to increased kinetic energies of individual carriers and carrier scattering rates, thereby promoting the process of carrier thermalization.[46] However, in practical scenarios, it is necessary to account for the light absorption characteristics of the entire film. By measuring the thickness-dependent absorptance (Figure S22, Supporting Information), it was found that a thickness of ≈130 nm is a critical thickness for just perfect absorption for 320 nm laser. Here, the average film thickness for fabricating PDs was ≈250 nm. For thermal imaging measurements using films with a thickness of 250 nm, 320 nm photons can only penetrate nearly half the film thickness, not enough to heat the entire film. For 360 nm photons with larger energies, they can be absorbed by the films more effectively, resulting in the maximum temperature change. Besides, the trend of temperature variation versus laser wavelength is consistent with the spectral photoresponses in Figure S15, Supporting Information, proving that the pyro–phototronic effect causes the current spikes of the PDs. For photoresponses measurements, the absorption of ITO also influences the photoresponses of the PDs. From the transmission spectrum of the ITO glass in Figure S23, Supporting Information, one can see that ITO can strongly absorb the 320 nm light with a transmittance of 43%. While for 360 nm, the transmittance is close to 80%. Most of the 320 nm photons can't be absorbed by perovskite films, leading to the weaker photoresponse than 360 nm laser. The time-dependent *It* curves in Figure 3e show highly repeatable and stable photoresponses under 360 nm laser illumination (0 V, 127 μW cm^{-2}). The pyroelectric response behavior in Figure 3e can be explained by the working mechanism of the ferro–pyro–phototronic effect in the schematic diagram (Figure 3f) and the energy band diagram in Figure 3g,h. In the equilibrium state (Figure 1d), a heterojunction is formed between 2D perovskite film and PC61BM, with the positive polar charges located at the interface between perovskite and PC61BM and the negative charges located at the interface between perovskite and ITO. To maintain electric neutrality, the holes in the ITO side and the electrons in the PC61BM side act as compensating charges. The depletion layer at the interface between perovskite and PC61BM is a barrier to prevent the recombination of the compensating charges. Under dark conditions, only dark current existed when an external circuit was formed. Due to the photo-excitation, the electron–hole pairs were generated and driven by the built-in electric field, generating the photocurrent (I_{photo}) when the laser was turned on. In the meantime, the photothermal effect induced by light absorption led to the temperature rise of the PDs. Therefore, the temperature rise induced by laser illumination led to a decrease in the intensity of ferroelectric polarization within the 2D ferroelectric perovskite film. Hence, the charge redistribution occurred, generating a positive pyroelectric current flow (I_{pyro}) from the ITO electrode to the Ag electrode through the external circuit. The total output current was defined as $I_{photo+pyro}$. When the temperature kept unchanged, the intensity of ferroelectric polarization no longer changed; thus, leaving only a photocurrent platform. Finally, when the laser was turned off, the cooling of the PDs led to the increase of ferroelectric polarization, along with the vanish of photocurrent.

Based on the ferro–pyro–phototronic effect, the figures of merit of the three PDs based on BA_2, $BDA_{0.7,}$ and BDA film were carefully examined. **Figure 4**a shows the *I*–*V* curves of the three PDs under light illumination, among which the $BDA_{0.7}$ one possessed the highest V_{oc} and highest photocurrents. The $I_{photo+pyro}$ as a function of power density for the three PDs is presented in Figure 4b in which one can see that the $BDA_{0.7}$ film-based PDs show much higher output currents than other PDs. As shown in Figure 4c, the response times of $BDA_{0.7}$ film-based PDs are determined as 270 μs for the rise and 920 μs for decay under 360 nm laser with a power density of 0.4 mW cm^{-2}, faster than the BA_2 film-based PD but a little slower than the BDA film-based PD. The corresponding responsivities (*R*) are shown in Figure 4d, where all three *R* show a decreasing tendency as a function of power density. The *R* and detectivity (*D**) were calculated following the equations below:

$$R = \frac{\left(I_{photo} - I_d\right)/S}{P} \tag{3}$$

$$D^* = \frac{(BS)^{1/2}}{NEP} = \frac{R(BS)^{1/2}}{\overline{i_n^2}^{1/2}} \tag{4}$$

where I_{photo} is the photocurrent, I_d is the dark current, *S* is the active area, *P* is the light power density, *B* is the bandwidth, NEP is the noise equivalent power, and $\overline{i_n^2}^{1/2}$ is the root mean square value of the noise current. Here, the noise currents of the three PDs were obtained by doing a Fourier transform of the dark currents[47] plotted in Figure S24a–c, Supporting Information, among which the $BDA_{0.7}$ film demonstrated the lowest dark current of $\approx 2.65 \times 10^{-12}$ A at 0 V bias. As shown in Figure S24d–f; Supporting Information, the noise current of the $BDA_{0.7}$ film PD at a bandwidth of 1 Hz is $\approx 2.3 \times 10^{-15}$ A $Hz^{-1/2}$. Besides, for all three PDs, the noise current depends on the frequency, indicating that the $1/f$ noise dominates the noise currents. To evaluate the average responsivities and detectivities of the three PDs, the statistics of device performance were conducted by measuring $I_{photo+pyro}$ under 360 nm illumination with the lowest power density (1 nW for our measurements) from ten different devices. As shown in Figure 4e, the $BDA_{0.7}$ film-based self-powered PD presents a high average *R* of 89.2 ± 1.8 A W^{-1} and corresponding *D** of 2.25×10^{15} Jones (cm $Hz^{1/2}$ W^{-1}), much higher than the BA_2 or BDA film-based PDs. Such excellent performances can be

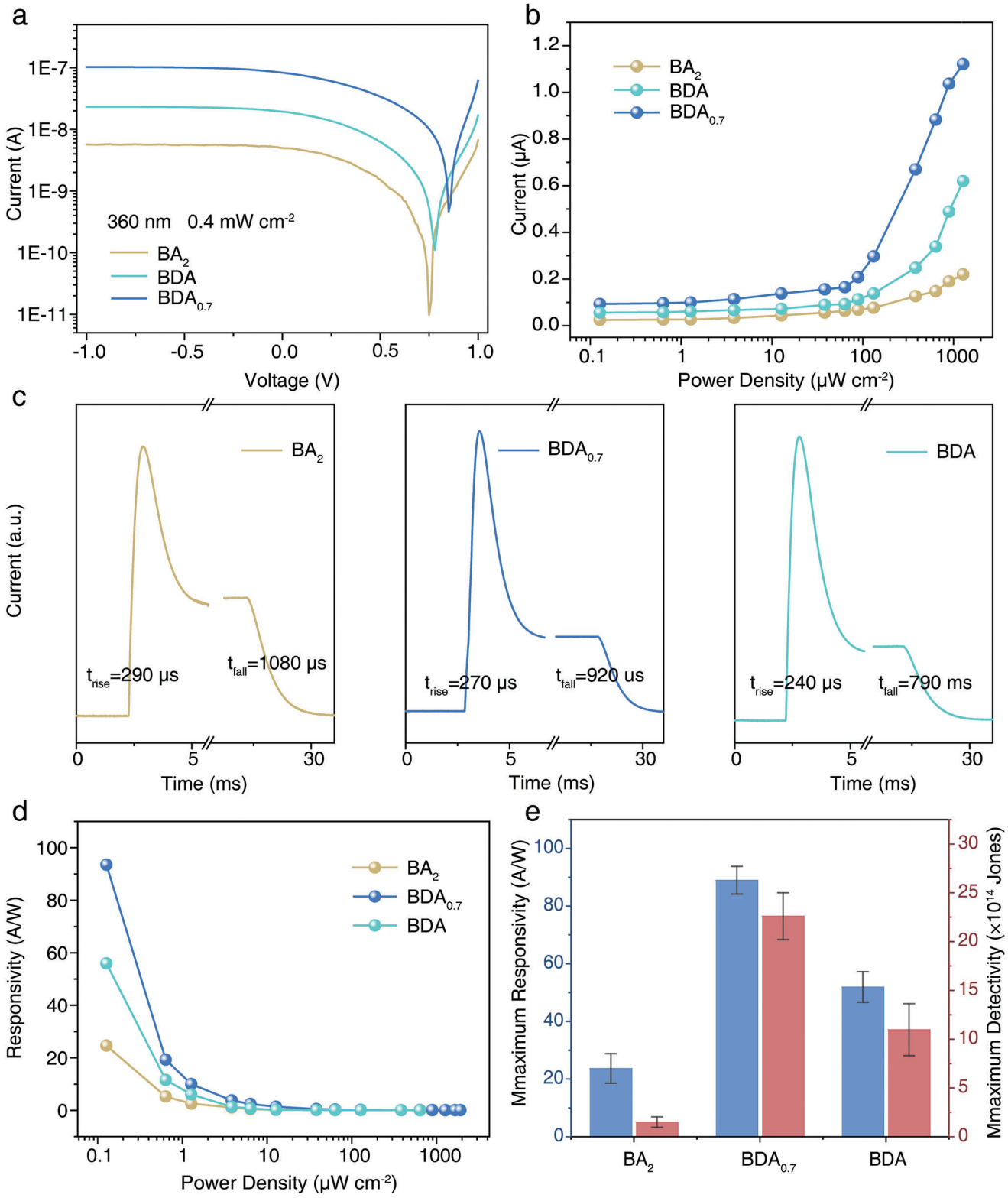

Figure 4. Comparison of performance of PDs based on BA_2, $BDA_{0.7}$, and BDA films. a) *I–V* curves of PDs under laser illumination conditions with a power density of 0.4 mW cm^{-2}. b) Power density-dependent output currents of the three PDs measured under an on–off frequency of 0.2 Hz. c) Temporal responses of three PDs. d) Power density-dependent responsivities of the three PDs measured under an on–off frequency of 0.2 Hz. e) Statistics of maximum responsivities and detectivities of three PDs.

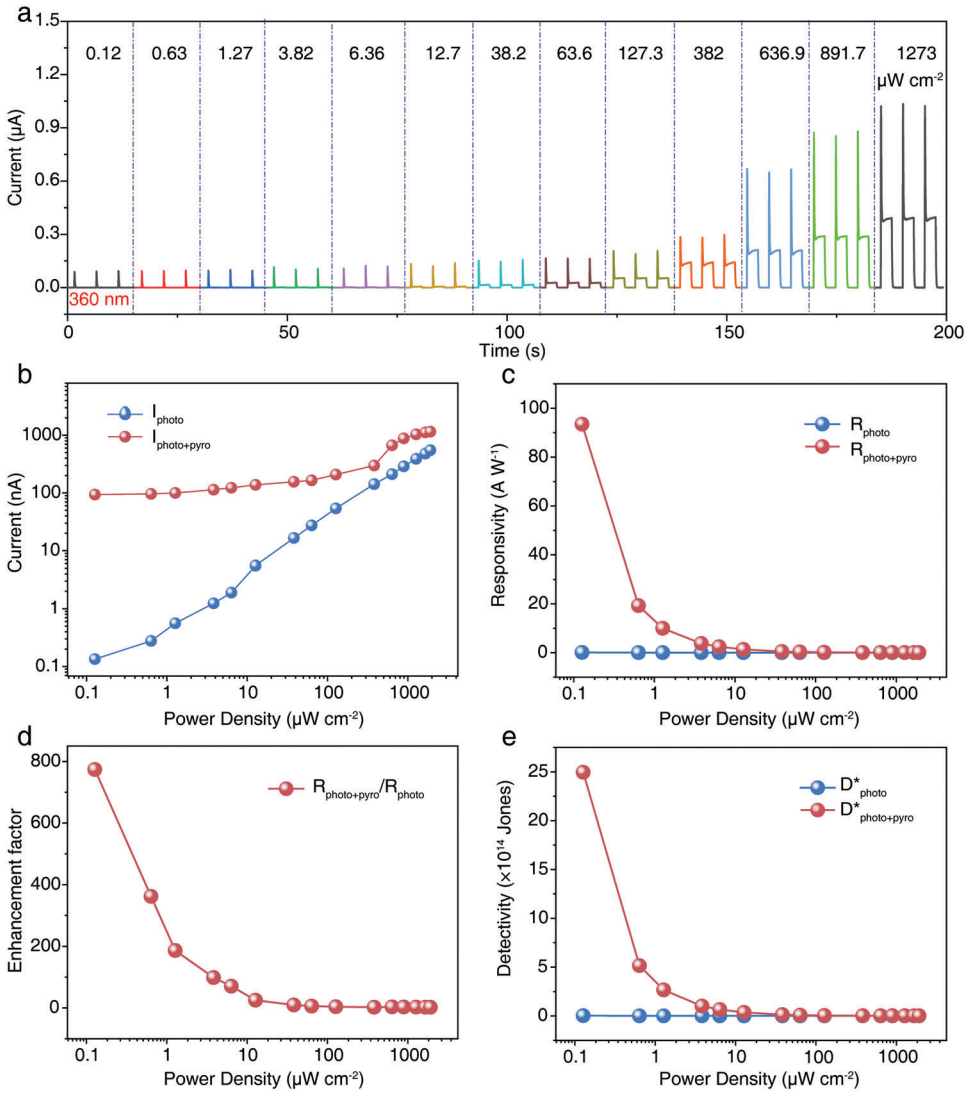

Figure 5. Self-powered performance of the interfacial pyroelectric effect enhanced PD toward 360 nm laser. a) Photoresponses of the PD with different power densities from 0.12 to 1273 μW cm^{-2}. Two output currents b) extracted from the corresponding responsivities (a) and c) corresponding detectivities of e) the PD as a function of the power density. d) Enhancement factor for $(R_{pyro+photo})/R_{photo}$ and $R_{pyro+photo}/R_{photo}$.

attributed to the low trap density, high ordered orientation, and good ferroelectricity of the $BDA_{0.7}$ film. Therefore, all the photoresponse performances above prove the advancement of the 2D perovskite ferroelectric films with mixed spacer cations.

Further, the overall performances of the $BDA_{0.7}$ film-based PD toward the 360 nm laser were measured and plotted in **Figure 5**. As shown in Figure 5a, all the on–off photoresponses of the PD at 0 bias under 360 nm laser with power density ranging from 0.12 to 1273 μW cm^{-2} demonstrate transient pyroelectric output currents. Under low power densities (0.12–6.36 μW cm^{-2}), no evident photocurrent plateaus were found, accompanied by obvious pyroelectric currents. Then, the $I_{photo+pyro}$ and I_{photo} extracted from Figure 5a were plotted in Figure 5b as a function of the power density. Both output currents monotonously increased with the increase of the power density. The photocurrents showed a nearly linear response from 0.12 to 1273 μW cm^{-2}, quite different from the power density-dependent increasing trend of pyroelectric currents. Then, the R and D^* were calculated and plotted in Figures 5c and 5e, respectively, as a function of power density. Both the R and D^* tended to decrease rapidly with the increase of the power density due to the higher charge recombination rate under higher illumination intensity. Moreover, the ferro–pyroelectric effect could significantly increase the ability of the self-powered PDs toward light with low power density. As shown in Figure 5d, the pyroelectric currents increased the output currents, with a maximum enhancement of ≈800 compared with the photocurrent plateau. The enhancement factor was larger than 100 with a power density of less than 4 μW cm^{-2}. The maximum R and D^* were obtained with a value of 89.2 ± 1.8 A W^{-1} and 2.25 × 10^{15} Jones, respectively, at the lowest intensity of 0.12 μW cm^{-2}. In addition, the overall performances of the BA_2 film and BDA film-based PDs toward 360 nm laser were measured and plotted in Figures S25 and S26, Supporting Information, respectively. Figure S27, Supporting Information shows

the averaged maximum R and D^* of the PDs based on the $BDA_{0.7}$ film with good repeatability, behaving with small performance distribution. In addition, we evaluated the impact of several factors such as bias voltage, light switching frequency, temperature change rate, and operating temperature on the performances of the PDs because they can influence the ferro–pyro–phototronic effect. The corresponding results are shown in Figures S28–S31, Supporting Information, respectively. Figure S28, Supporting Information shows that the pyroelectric currents will vanish when bias voltage (either positive bias or reversed bias) exceeds 1 V. The frequency-dependent rise/fall times are shown in Figure S29b, Supporting Information, showing the faster response and recovery speeds with the increase of light-switching frequency. Figure S30, Supporting Information shows the pyroelectric responses toward a change of temperature using a 10.6 μm laser as the heating source. Figure S31, Supporting Information shows the temperature dependence of the ferro–pyro–phototronic effect in $BDA_{0.7}$ film-based PD. With the increased operating temperature, the output currents undergo a continuous declination. The pyroelectric current would vanish between 357 and 378 K, just covering the curie temperature of 371 K, as shown in Figure S13, Supporting Information. In other words, the disappearance of ferroelectricity leads to the vanishing of pyroelectric currents. The above results demonstrate the high-temperature dependence of the ferro–pyro–phototronic effect. In addition, the reversible property of spontaneous polarization allows the modulation of the output current by applying polarization voltage in the opposite direction (Figure S32, Supporting Information). Furthermore, as EA^+ can either act as an L or A cation, and doping of MA^+ may influence the composition of the final films, hybrid perovskites such as $BA_2EA_2Pb_3Br_{10}$, $EA_2MA_2Pb_3Br_{10}$, and $BA_2MA_2Pb_3Br_{10}$ may exist in the $BDA_{0.7}$ film, which may dominate the performance of the final PDs. Therefore, we prepared another two perovskite films, with the structural formula of $EA_2MA_2Pb_3Br_{10}$ and $BDA_{0.7}BA_{0.6}MA_2Pb_3Br_{10}$, respectively, using the same spin-coating process. Figure S33a,c,e, Supporting Information plots the I–t curves of the $BDA_{0.7}BA_{0.6}EA_2Pb_3Br_{10}$ film, $EA_2MA_2Pb_3Br_{10}$ film, and $BDA_{0.7}BA_{0.6}MA_2Pb_3Br_{10}$ film-based PDs, respectively. The corresponding $I_{pyro+photo}$ and I_{photo} are extracted and plotted in Figure S33b,d,f, Supporting Information as a function of power density. Although the $EA_2MA_2Pb_3Br_{10}$ film-based PD shows pyroelectric photoresponse behaviors, the output currents are over two orders of magnitude smaller than the $BDA_{0.7}BA_{0.6}EA_2Pb_3Br_{10}$ film-based PD. For the $BDA_{0.7}BA_{0.6}MA_2Pb_3Br_{10}$ film, as this perovskite is nonferroelectric, no pyroelectric responses were observed. In addition, the photocurrents of $BDA_{0.7}BA_{0.6}MA_2Pb_3Br_{10}$ film-based PD are much smaller than the $BDA_{0.7}BA_{0.6}EA_2Pb_3Br_{10}$ film-based one. For another possible component of $BA_2MA_2Pb_3Br_{10}$, the performances of the $BA_2MA_2Pb_3Br_{10}$ film-based PD can be seen in our previous report,[37] with the peak R of 0.4 A W^{-1}, much lower than that of the $BDA_{0.7}BA_{0.6}EA_2Pb_3Br_{10}$ film-based PD, as high as 93 A W^{-1}. From the above results, we can determine that the ferroelectric phase $BDA_{0.7}BA_{0.6}MA_2Pb_3Br_{10}$ rather than other components played a decisive role in self-powered photoresponses. Moreover, we fabricated the PD based on $BDA_{0.7}BA_{0.6}EA_2Pb_3Br_{10}$ film prepared without MAAc. The on–off photoresponses of the PD w/o MAAc at 0 bias under 360 nm laser with power density ranging from 0.12 to 636.9 μW cm^{-2} are shown in Figure S34a, Supporting Information. Figure S34b,c, Supporting Information compares the $I_{pyro+photo}$ and $R_{pyro+photo}$, respectively, from which one can see that the introduction of MAAc significantly improves the overall performances of the PDs. This is due to the enhanced crystallinity and phase purity. In addition, a peak R of 7 A W^{-1} is still much higher than those of $EA_2MA_2Pb_3Br_{10}$ film, $BA_2MA_2Pb_3Br_{10}$, and $BDA_{0.7}BA_{0.6}MA_2Pb_3Br_{10}$ film-based ones.

As the $BDA_{0.7}$ film shows ferroelectric properties, a combination of ferroelectricity and piezoelectricity is an excellent strategy to further boost the performances of PDs utilizing the piezo–phototronic effect.[13,48] Therefore, the photoresponses of the $BDA_{0.7}$ film-based PDs modulated by the piezo–phototronic effect under 360 nm illumination were systematically studied. The vertical pressures were applied using a homemade device (**Figure 6**a). The pressures were modulated by a moving stage and measured by a digital push and pull tester (HP-50). First, the I–V characteristics of the PD under different pressures with a 360 nm laser power density of 300 μW cm^{-2} were measured and shown in Figure 6b. The photocurrent first increases and then decreases with the increase of compressive pressure. Then, the photoresponses of the PD toward 360 nm laser with different power densities (0.12, 127, and 1273 μW cm^{-2}) under different pressures were measured and plotted in Figure 6c; Figure S35, Supporting Information, respectively. For all three power densities, the pyroelectric currents and photocurrents increased with the pressure increase from 0 to 45 kPa; and thus, decreased with further increasing the pressure to 60 kPa, showing the effective modulation of piezo–phototronic effect on the ferro–pyro–phototronic effect (Figure S36a, Supporting Information). The corresponding pressure-modulated $R_{pyro+photo}$ and R/R_0 ratios (R_0 is the responsivity without pressure) are shown in Figures 6d and 6e, respectively. Under a pressure of 45 kPa, $R_{pyro+photo}$ with a power density of 0.12 μW cm^{-2} could be significantly enhanced from 89 to 497 A W^{-1} when a pressure of 45 kPa was applied and further decreased to 234 A W^{-1} when further increasing to 60 kPa. For the other two power densities (127 and 1273 μW cm^{-2}), peak responsivities were also obtained under a pressure of 45 kPa. The highest $R_{pyro+photo}$ enhancement ratio was as high as 480% under a pressure of 45 kPa with a low power density (0.12 μW cm^{-2}). The enhancement ratio decreased with the increase of power density, reaching to 234% under a pressure of 45 kPa with a higher power density (1273 μW cm^{-2}). The corresponding pressure-dependent D^* is shown in Figure S36b, Supporting Information. In addition, the piezo–phototronic effect can greatly modulate the photocurrent plateau, with the corresponding results shown in Figure S37, Supporting Information. The performances of our PDs and those of previously reported perovskite-based self-powered PDs are compared and summarized in Table S3, Supporting Information, showing that our PDs demonstrate the highest photoresponsivity, detectivity, and comparable response/recovery times. The working mechanism of the modulation function of the piezo–phototronic effect under pressure can be explained by schematic energy band diagrams in Figure S38, Supporting Information. Compared with pressure-free conditions (Figure S34a, Supporting Information), when a moderate compressive pressure was applied to the PD, positive and negative piezoelectric polarization charges were generated at the interface between 2D perovskite/PC61BM and

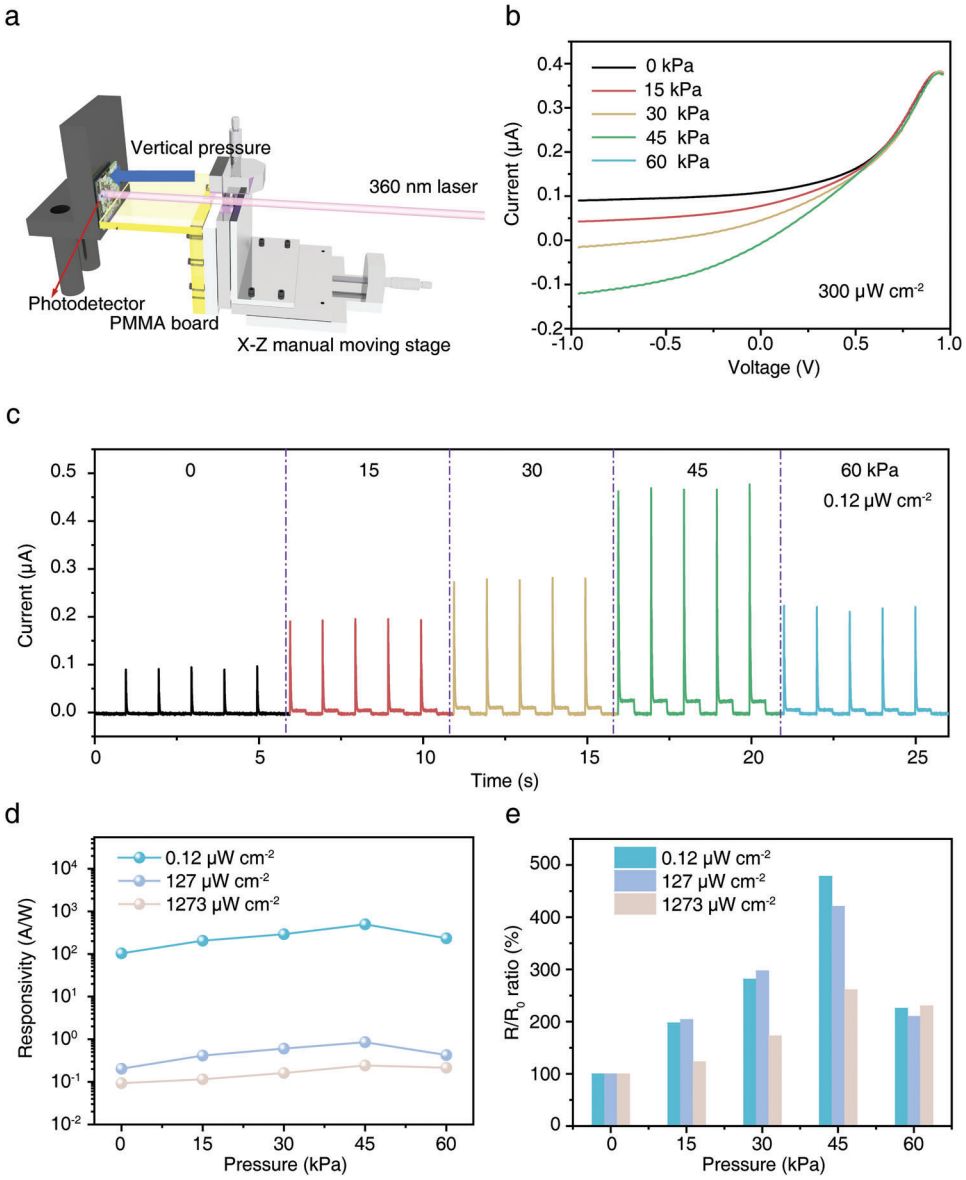

Figure 6. The piezo–phototronic effect of the enhanced performance of the $BDA_{0.7}$ film-based PDs. a) The schematic diagram shows how pressures were applied to the PDs. b) *I–V* curves of PDs under laser illumination conditions with a power density of 300 μW cm^{-2}, applied with different vertical pressures. c) *I–t* photoresponses of the PD under different compressive pressures, with a power density of 0.12 μW cm^{-2}. d) Responsivity of the PDs as a function of pressure, with power densities of 0.12, 127, and 1273 μW cm^{-2}, respectively. e) Corresponding pressure dependence of enhancement ratio of *R* with three power densities.

2D perovskite/ITO, respectively, attracting the electrons moving toward and repelling the holes away from the heterojunction interface. Therefore, a downward bending of the energy band occurred at the interface between perovskite and PC61BM, which could enhance the built-in electric field, beneficial for separating photogenerated carriers and reducing carrier recombination. Besides, the piezo-charges at the interface induced by pressures were consistent with the ferroelectric-induced bound charges. Therefore, the pyroelectric currents were greatly enhanced due to the strengthened positive pyro-potential. However, when pressure was larger than 60 kPa, excessive piezo-charges were generated at the heterojunction interface, leading to the further downward bending of the conduction band of the perovskite film. Thus, the bottom of the conduction band of the perovskite film became lower than the HOMO level of PC61BM. Therefore, a band misalignment was generated at the interfaces,[49,50] hindering the charge carriers' transport and decreasing the $I_{photo+pyro}$ and I_{photo}. However, when a negative polarization voltage was applied, the increased compressive pressure would decrease output currents (Figure S39, Supporting Information). This may be due to the negative piezoelectric polarization charges resulting in the upward bending of the energy band at the interface between perovskite and PC61BM, which could impair the built-in electric field, bad for the separation

and transport of photogenerated carriers. The above results demonstrate the superiority of coupling the ferro–pyro–phototronic effect and piezo–phototronic effect to boost the performances of self-powered PDs.

The long-term stability of humidity and heating treatment is crucial for MHP-based devices. Before humidity stability measurements, the water resistance of the three perovskite films was evaluated by comparing the time-dependent contact angles (Figure S40, Supporting Information. One can see that the initial water contact angle on the surface of $BDA_{0.7}$ film (149°) was larger than that for BA_2 film (120.8°) and much larger than that for BDA film (83.6°), indicating the increased hydrophobicity with the mixing of BA^+ and BDA^{2+}. Besides, the water contact angle on the surface of BA_2 film had significantly decayed from 120.8° to 82.2° in 120 s; while, the $BDA_{0.7}$ film could hold a contact angle larger than 100° during the same period, confirming that the perovskite film with mixed spacer cations demonstrates the strongest water resistance. Further, the long-term humidity stability and thermal stability measurements of the three kinds of PDs were conducted. Figure suppinfo1, Supporting Information shows that the mixed film combines the virtues of the RP-type and DJ-type 2D perovskite. When heated at 80 °C for 38 days, the BA_2 film-based PD showed the worst thermal stability, with a decay of more than 40% photoresponse of the initial value. While for the $BDA_{0.7}$ film-based PD, the best thermal stability was obtained, with a decay of less than 20% photoresponse of the initial value within 38 days, slightly better than the BDA film-based PD. When stored in a moist atmosphere (relative humidity of 80% ± 5%, room temperature), the photoresponse of the BDA film-based PDs rapidly decayed to less than 55% of the initial value within 38 days. In addition, the mixed film-based PD maintained 80% of the initial value after 38 days of exposure to humidity, showing the best humidity stability. The corresponding photoresponses of the PDs based on $BDA_{0.7}$ film, BA_2 film, and BDA film to 360 nm laser with the same intensity after 0, 18, and 38 days of exposure to humidity or thermal treatment are shown in Figures S41,S42, Supporting Information, respectively. Therefore, from the results above, humidity and thermal stability are greatly enhanced by mixing the RP-type and DJ-type perovskites.

3. Conclusion

In summary, 2D ferroelectric perovskite films with vertical orientation, high crystallinity, and high phase purity were prepared by mixing the RP-type ferroelectric perovskite and DJ-type ferroelectric perovskite in the precursor solutions. The optimized $(BDA_{0.7}(BA_2)_{0.3})(EA)_2Pb_3Br_{10}$ film demonstrated the desirable microscopic surface morphology, best crystallinity, lowest trap densities, and uniformly distributed quantum wells. Besides, both *P–E* loops and PFM measurements confirmed the ferroelectric feature in $(BDA_{0.7}(BA_2)_{0.3})(EA)_2Pb_3Br_{10}$ films, beneficial for fabricating high-performance self-powered PD. Consequently, by using the ferro–pyro–phototronic effect, self-powered UV PDs based $(BDA_{0.7}(BA_2)_{0.3})(EA)_2Pb_3Br_{10}$ film demonstrated excellent performance, with the dark current less than 3×10^{-12} A, peak response more than 93 A W^{-1}, and a detectivity of 2.5×10^{15} Jones, together with the excellent reproducibility and stability. The piezo–phototronic effect can be further coupled with the ferro–pyro–phototronic effect to boost performance. Under a pressure of 45 kPa, $R_{pyro+photo}$ with a power density of 0.12 μW cm^{-2} can be significantly enhanced from 89 to 497 A W^{-1}, with an enhancement ratio as high as 480%. Our results offer an effective approach for preparing high-performance 2D perovskite ferroelectric films and resultant self-powered PDs and provide strategies for further exploration of new ferroelectrics for diversified optoelectronic applications.

Supporting Information

Supporting Information is available from the Wiley Online Library or from the author.

Acknowledgements

L.G., Y.Q., and Z.W. contributed equally to this work. This work was supported by the National Natural Science Foundation of China (Grant Nos. U20A20166, 62005072, and 62104057), the Natural Science Foundation of Hebei Province (Grant No. E2021201016), the Hebei Education Department (Grant No. BJK2022050), the Advanced Talents Incubation Program of the Hebei University (Grant Nos. 521000981351 and 521000981248), and the Science and Technology Plan Project of Hebei Province (Grant Nos. 226Z1002G and 226Z1703G).

Conflict of Interest

The authors declare no conflict of interest.

Data Availability Statement

Research data are not shared.

Keywords

ferroelectric film, ferro–pyro–phototronic effect, mixed 2D perovskites, piezo–phototronic effect, self-powered photodetectors

Received: February 21, 2023
Revised: July 30, 2023
Published online:

[1] H. Wang, D. H. Kim, *Chem. Soc. Rev.* **2017**, *46*, 5204.
[2] W. Liu, J. Lv, L. Peng, H. Guo, C. Liu, Y. Liu, W. Li, L. Li, L. Liu, P. Wang, S. C. Bodepudi, K. Shehzad, G. Hu, K. Liu, Z. Sun, T. Hasan, Y. Xu, X. Wang, C. Gao, B. Yu, X. Duan, *Nat. Electron.* **2022**, *5*, 281.
[3] Y. Liu, Y. Zhang, X. Zhu, Z. Yang, W. Ke, J. Feng, X. Ren, K. Zhao, M. Liu, M. G. Kanatzidis, S. F. Liu, *Sci. Adv.* **2021**, *7*, 8844.
[4] M. Kumar, H. Seo, *Adv. Mater.* **2022**, *34*, 2106881.
[5] Y. Heo, M. Alexe, *Adv. Mater.* **2022**, *34*, 2105845.
[6] S. Wang, L. Li, W. Weng, C. Ji, X. Liu, Z. Sun, W. Lin, M. Hong, J. Luo, *J. Am. Chem. Soc.* **2020**, *142*, 1703694.
[7] N. Ma, K. Zhang, Y. Yang, *Adv. Mater.* **2017**, *29*, 1703694.
[8] Z. Wang, R. Yu, C. Pan, Z. Li, J. Yang, F. Yi, Z. L. Wang, *Nat. Commun.* **2015**, *6*, 8401.
[9] Y. Zhang, J. Chen, L. Zhu, Z. L. Wang, *Nano Lett.* **2021**, *21*, 8808.
[10] Y. Zhang, Y.-C. Wang, L. Wang, L. Zhu, Z. L. Wang, *Adv. Mater.* **2022**, *34*, 2204363.

[11] Q. Li, J. Meng, J. Huang, Z. Li, *Adv. Funct. Mater.* **2021**, *32*, 2108903.
[12] Y. Liu, X. Pan, X. Liu, S. Han, J. Wang, L. Lu, H. Xu, Z. Sun, J. Luo, *Small* **2022**, *18*, 2106888.
[13] R. Ding, Y. Lyu, Z. Wu, F. Guo, W. F. Io, S.-Y. Pang, Y. Zhao, J. Mao, M.-C. Wong, J. Hao, *Adv. Mater.* **2021**, *33*, 2101263.
[14] K. Maity, U. Pal, H. K. Mishra, P. Maji, P. Sadhukhan, Z. Mallick, S. Das, B. Mondal, D. Mandal, *Nano Energy* **2022**, *92*, 106743.
[15] Z. Yang, H. Wang, L. Guo, Q. Zhou, Y. Gu, F. Li, S. Qiao, C. Pan, S. Wang, *Small* **2021**, *17*, 2101572.
[16] C. Chen, J. Chen, H. Han, L. Chao, J. Hu, T. Niu, H. Dong, S. Yang, Y. Xia, Y. Chen, W. Huang, *Nature* **2022**, *612*, 266.
[17] J. Jeong, M. Kim, J. Seo, H. Lu, P. Ahlawat, A. Mishra, Y. Yang, M. A. Hope, F. T. Eickemeyer, M. Kim, Y. J. Yoon, I. W. Choi, B. P. Darwich, S. J. Choi, Y. Jo, J. H. Lee, B. Walker, S. M. Zakeeruddin, L. Emsley, U. Rothlisberger, A. Hagfeldt, D. S. Kim, M. Grätzel, J. Y. Kim, *Nature* **2021**, *592*, 381.
[18] J. S. Kim, J.-M. Heo, G.-S. Park, S.-J. Woo, C. Cho, H. J. Yun, D.-H. Kim, J. Park, S.-C. Lee, S.-H. Park, E. Yoon, N. C. Greenham, T.-W. Lee, *Nature* **2022**, *611*, 688.
[19] X. Feng, Y. He, W. Qu, J. Song, W. Pan, M. Tan, B. Yang, H. Wei, *Nat. Commun.* **2022**, *13*, 6106.
[20] S. Shahrokhi, W. Gao, Y. Wang, P. R. Anandan, M. Z. Rahaman, S. Singh, D. Wang, C. Cazorla, G. Yuan, J.-M. Liu, T. Wu, *Small Methods* **2020**, *4*, 2000149.
[21] W. Zheng, X. Wang, X. Zhang, B. Chen, H. Suo, Z. Xing, Y. Wang, H.-L. Wei, J. Chen, Y. Guo, F. Wang, *Adv. Mater.* **2022**, *35*, 2205410.
[22] Y. Lei, Y. Li, C. Lu, Q. Yan, Y. Wu, F. Babbe, H. Gong, S. Zhang, J. Zhou, R. Wang, R. Zhang, Y. Chen, H. Tsai, Y. Gu, H. Hu, Y.-H. Lo, W. Nie, T. Lee, J. Luo, K. Yang, K.-I. Jang, S. Xu, *Nature* **2022**, *608*, 317.
[23] A. G. Ricciardulli, S. Yang, J. H. Smet, M. Saliba, *Nat. Mater.* **2021**, *20*, 1325.
[24] X. Li, J. M. Hoffman, M. G. Kanatzidis, *Chem. Rev.* **2021**, *121*, 2230.
[25] Y. Liu, Y. Zhang, Z. Yang, H. Ye, J. Feng, Z. Xu, X. Zhang, R. Munir, J. Liu, P. Zuo, Q. Li, M. Hu, L. Meng, K. Wang, D.-M. Smilgies, G. Zhao, H. Xu, Z. Yang, A. Amassian, J. Li, K. Zhao, S. Liu, *Nat. Commun.* **2018**, *9*, 5302.
[26] L. Guo, X. Liu, L. Gao, X. Wang, L. Zhao, W. Zhang, S. Wang, C. Pan, Z. Yang, *ACS Nano* **2022**, *16*, 1280.
[27] J. Feng, C. Gong, H. Gao, W. Wen, Y. Gong, X. Jiang, B. Zhang, Y. Wu, Y. Wu, H. Fu, L. Jiang, X. Zhang, *Nat. Electron.* **2018**, *1*, 404.
[28] P.-P. Shi, Y.-Y. Tang, P.-F. Li, W.-Q. Liao, Z.-X. Wang, Q. Ye, R.-G. Xiong, *Chem. Soc. Rev.* **2016**, *45*, 3811.
[29] C.-F. Wang, H. Li, M.-G. Li, Y. Cui, X. Song, Q.-W. Wang, J.-Y. Jiang, M.-M. Hua, Q. Xu, K. Zhao, H.-Y. Ye, Y. Zhang, *Adv. Funct. Mater.* **2021**, *31*, 2009457.
[30] Y. Yang, F. Lou, H. Xiang, *Nano Lett.* **2021**, *21*, 3170.
[31] H. Ye, Y. Peng, X. Shang, L. Li, Y. Yao, X. Zhang, T. Zhu, X. Liu, X. Chen, J. Luo, *Adv. Funct. Mater.* **2022**, *32*, 2200223.
[32] W.-Q. Liao, Y. Zhang, C.-L. Hu, J.-G. Mao, H.-Y. Ye, P.-F. Li, S. D. Huang, R.-G. Xiong, *Nat. Commun.* **2015**, *6*, 7338.
[33] S. Han, M. Li, Y. Liu, W. Guo, M.-C. Hong, Z. Sun, J. Luo, *Nat. Commun.* **2021**, *12*, 284.
[34] A. Z. Chen, M. Shiu, J. H. Ma, M. R. Alpert, D. Zhang, B. J. Foley, D.-M. Smilgies, S.-H. Lee, J. J. Choi, *Nat. Commun.* **2018**, *9*, 1336.
[35] S. Sidhik, Y. Wang, M. De Siena, R. Asadpour, A. J. Torma, T. Terlier, K. Ho, W. Li, A. B. Puthirath, X. Shuai, A. Agrawal, B. Traore, M. Jones, R. Giridharagopal, P. M. Ajayan, J. Strzalka, D. S. Ginger, C. Katan, M. A. Alam, J. Even, M. G. Kanatzidis, A. D. Mohite, *Science* **2022**, *377*, 1425.
[36] L. Min, W. Tian, F. Cao, J. Guo, L. Li, *Adv. Mater.* **2021**, *33*, 2101714.
[37] L. Guo, Y. Qi, Z. Yang, L. Zhao, W. Zhang, X. Wang, H. Liu, G. Yan, S. Wang, C. Pan, *Nano Energy* **2022**, *102*, 107714.
[38] L. Cheng, K. Meng, Z. Qiao, Y. Zhai, R. Yu, L. Pan, B. Chen, M. Xiao, G. Chen, *Adv. Mater.* **2022**, *34*, 2106380.
[39] H. Yu, Y. Xie, J. Zhang, J. Duan, X. Chen, Y. Liang, K. Wang, L. Xu, *Adv. Sci.* **2021**, *8*, 2004510.
[40] C. Ji, S. Wang, Y. Wang, H. Chen, L. Li, Z. Sun, Y. Sui, S. Wang, J. Luo, *Adv. Funct. Mater.* **2019**, *30*, 1905529.
[41] R. Xu, H. Dong, P. Li, X. Cao, H. Li, J. Li, Z. Wu, *ACS Appl. Mater. Interfaces* **2021**, *13*, 33218.
[42] H. Tsai, W. Nie, J.-C. Blancon, C. C. Stoumpos, R. Asadpour, B. Harutyunyan, A. J. Neukirch, R. Verduzco, J. J. Crochet, S. Tretiak, L. Pedesseau, J. Even, M. A. Alam, G. Gupta, J. Lou, P. M. Ajayan, M. J. Bedzyk, M. G. Kanatzidis, A. D. Mohite, *Nature* **2016**, *536*, 312.
[43] Z. Xu, D. Lu, X. Dong, M. Chen, Q. Fu, Y. Liu, *Adv. Mater.* **2021**, *33*, 2105083.
[44] Y. Zhang, M. Chen, T. He, H. Chen, Z. Zhang, H. Wang, H. Lu, Q. Ling, Z. Hu, Y. Liu, Y. Chen, G. Long, *Adv. Mater.* **2023**, *35*, 2210836.
[45] X. Cui, Q. Ruan, X. Zhuo, X. Xia, J. Hu, R. Fu, Y. Li, J. Wang, H. Xu, *Chem. Rev.* **2023**, *123*, 6891.
[46] J. Fu, S. Ramesh, J. W. Melvin Lim, T. C. Sum, *Chem. Rev.* **2023**, *123*, 8154.
[47] C.-H. Liu, Y.-C. Chang, T. B. Norris, Z. Zhong, *Nat. Nanotechnol.* **2014**, *9*, 273.
[48] L. Guo, X. Liu, R. Cong, L. Gao, K. Zhang, L. Zhao, X. Wang, R.-N. Wang, C. Pan, Z. Yang, *Nano Lett.* **2022**, *22*, 8241.
[49] Q. Lai, L. Zhu, Y. Pang, L. Xu, J. Chen, Z. Ren, J. Luo, L. Wang, L. Chen, K. Han, P. Lin, D. Li, S. Lin, B. Chen, C. Pan, Z. L. Wang, *ACS Nano* **2018**, *12*, 10501.
[50] C. W. Jang, H. Kim, M. K. Nazeeruddin, D. H. Shin, S.-H. Choi, *Nano Energy* **2021**, *84*, 105899.